Surface & Coatings Technology 344 (2018) 12–20

Contents lists available at ScienceDirect

Surface & Coatings Technology

journal homepage: www.elsevier.com/locate/surfcoat

Hydrogen plasma-enhanced atomic layer deposition of hydrogenated amorphous carbon thin films

Taejin Choi[a], Seungmin Yeo[a], Jeong-Gyu Song[a], Seunggi Seo[a], Byeonghyeon Jang[b], Soo-Hyun Kim[b], Hyungjun Kim[a,*]

[a] Nanodevice Laboratory, School of Electrical and Electronic Engineering, Yonsei University, Seodaemun-Gu, Seoul 120-749, Republic of Korea
[b] Nano-Devices and Process Laboratory, School of Materials Science and Engineering, Yeungnam University, Dae-Dong, Gyeongsan-Si 712-749, Republic of Korea

ARTICLE INFO

Keywords:
Hydrogenated amorphous carbon
Atomic layer deposition
Hydrogen plasma
Carbon tetrabromide
Substrate pretreatment

ABSTRACT

Hydrogenated amorphous carbon (a-C:H) thin films were prepared by hydrogen plasma-enhanced atomic layer deposition (PE-ALD). The a-C:H thin films were grown at low temperatures in the range of 150–350 °C using CBr_4 as the precursor and hydrogen plasma as the reactant. Raman spectroscopy, secondary ion mass spectrometry, X-ray photoelectron spectroscopy and Fourier transform infrared measurements showed that the a-C:H films consist of hydrogenated nanocrystalline sp^3 diamond, disordered sp^3 carbon and sp^2-hybridized graphitic carbon incorporated with oxygen as a main contaminant. Moreover, the incorporation of bromine and oxygen in the a-C:H films was significantly reduced upon increasing the growth temperature from 200 to 300 °C. Surface hydroxylation and precursor exposure pretreatments were employed to saturate the adsorption of CBr_4 precursors and enhance the initial nucleation of carbon during the deposition of the a-C:H thin film by the PE-ALD process. In addition, the conformal growth of a-C:H thin films on three-dimensional structures was confirmed.

1. Introduction

Carbon is one of the most abundant elements in nature and is found in different forms in a variety of carbon materials, such as graphite (sp^2-hybridized carbon), diamond (sp^3-hybridized carbon), and amorphous carbon (a-C, with randomly sp^2- and sp^3-hybridized carbon). Each form has unique physical and chemical properties, depending on its structure [1,2]. Among the different forms, the disordered (a-C) one is particularly attractive, owing to its electrical properties, chemical inertness, and good hardness. The structure of a-C is stabilized by saturating dangling bonds with hydrogen, forming hydrogenated amorphous carbon (a-C:H), which has important advantages such as low cost and ease of synthesis, which make it an attractive material for practical applications such as lubricating coatings and double patterning hard-masks, and secondary (rechargeable) sodium-ion battery electrodes [3–6]. Nanocrystalline graphitic carbon, as a type of a-C, consists of nanosized sp^2 graphitic carbon domains which are attributed to better electrical conductivity than other types of a-C. For this reason, nanocrystalline graphitic carbon has been used as a coating material for transparent conducting films and lithium-ion batteries [7,8].

Conformal and uniform deposition of carbon materials on various substrate structures and materials becomes more and more important to many research areas. For example, with the current continuous decrease in the feature size of integrated circuits in the semiconductor industry, achieving a close control of the dimensions and high step coverage of hard mask spacers comprising a-C:H is a key requirement in order to fabricate uniform and conformal pattern features in self-aligned double patterning technologies [9]. In addition, the uniform and conformal coating process of thickness-controlled graphitic carbon layer on electrode materials is also important for rechargeable battery technologies, because graphitic carbon layer can improve the surface chemistry of the electrode materials, provide good conductivity, and protect the electrodes from direct contact with electrolytes [10].

A large number of studies have reported the deposition of carbon by chemical vapor deposition (CVD) and physical vapor deposition (PVD) techniques, such as filtered cathodic arc, microwave plasma-assisted, and pulsed laser deposition, as well as filament-assisted CVD, reactive particle beam assisted sputtering, and electrodeposition, among the others [11–16]. However, achieving the growth of uniform and conformal carbon films on high aspect ratio structures such as holes and trenches using those conventional deposition methods has been very challenging, owing to the low step coverage and high growth temperatures typical of these approaches.

Atomic layer deposition (ALD) is considered a promising technique for the fabrication of nanomaterials, as it enables the deposition of a thin film with good uniformity over a large area [17,18]. The key

* Corresponding author.
E-mail address: hyungjun@yonsei.ac.kr (H. Kim).

https://doi.org/10.1016/j.surfcoat.2018.02.082
Received 6 September 2017; Received in revised form 16 February 2018; Accepted 21 February 2018
Available online 02 March 2018

advantages of the ALD technique include thickness control at the atomic scale, production of highly conformal films, and low-temperature growth [19]. Despite the high interest in carbon materials and the obvious potential of the ALD method for their preparation, there have been a few studies of the synthesis of any type of carbon using ALD. In 1993, Hukka et al. reported the atomic layer epitaxy (ALE) of diamond on a diamond (100) substrate by using chlorocarbon radicals and atomic hydrogen generated in a fluorine stream at a hot reactor [20]. In 1998, Komarov et al. also demonstrated the ALE of diamond films on Mo substrates using alternating fluxes of fluorocarbon radicals and atomic hydrogen generated in a hot filament reactor at high temperatures (over 700 °C) [21]. However, they did not achieve stable and reliable self-limiting growth for true ALD, and concluded that the growth process should be further optimized, for instance by investigating other halocarbon precursors and optimizing the ALD system. Recently, Zhang et al. demonstrated the ALD of graphene layers by using benzene precursor and hydrogen radical, showing layer-controlled and low temperature growth of high quality graphene by increasing ALD cycle [22]. However, the conformality of the graphene ALD on a nanostructure was not discussed, and the substrate material was limited to the copper foil as a growth catalyst.

The hydrogen plasma-enhanced ALD (PE-ALD) is a useful technique for the deposition of single-element films, especially at low deposition temperatures [23,24]. For example, hydrogen PE-ALD of semiconductors (Si and Ge) and metals (Ti, Cu, Ta, Ag, and Pd) has been performed using halide precursors, because of their high chemical reactivity with atomic hydrogen at low temperatures [25–31]. This same strategy should also enable the fabrication of carbon by PE-ALD using carbon halide precursors and atomic hydrogen: this would represent a very interesting approach with various potential applications. Among the possible carbon halide precursors, CBr_4 has a lower bond dissociation energy (approximately 234 kJ·mol^{-1} for the C—Br bond) compared with other halocarbon precursors (approximately 519 kJ·mol^{-1} for C—F bonds in CF_4 and 297 kJ·mol^{-1} for C—Cl bonds in CCl_4) and even aliphatic hydrocarbon precursors [32–35]. Furthermore, the good controllability and stability of the CBr_4 vapor flux near room temperature are also beneficial for ensuring a homogeneous supply of carbon [36]. For these reasons, CBr_4 has been frequently employed as a C dopant precursor to prepare compound semiconductors such as GaAs by molecular beam epitaxy [37,38]. Moreover, the bromocarbon molecules (CBr_4 or $CHBr_3$) are subsequently decomposed to bromomethyl radicals and HBr byproducts under atomic hydrogen, which highlights their relatively high reactivity with atomic hydrogen at low temperatures [32,37,39].

In this study, we report the growth of a-C:H thin films on a hydroxylated SiO_2 substrate by PE-ALD using CBr_4 and hydrogen plasma. Various experimental conditions, including substrate surface pretreatment, substrate temperature, and precursor injection time, were optimized to achieve self-limited ALD growth and excellent conformality of the a-C:H films. The thickness of the deposited a-C:H film was measured by spectroscopic ellipsometry and field-emission scanning electron microscopy (FE-SEM). The nanoscale surface profile of the a-C:H films were observed by an atomic force microscopy (AFM), whereas their chemical characterizations were performed by X-ray photoemission spectroscopy (XPS), secondary ion mass spectrometry (SIMS), Fourier transform infrared (FT-IR) spectroscopy and Raman spectroscopy. Also the electrical properties, such as field-effect mobility (μ_{eff}) and sheet resistance, were evaluated by the fabrication of back-gated a-C:H thin film transistors (C-TFTs).

2. Experimental

2.1. Experimental setup

The PE-ALD chamber used for depositing the a-C:H thin film consists of a showerhead-type injector and a capacitively coupled plasma (CCP) reactor with a 13.56 MHz radio frequency (rf) generator. The sample stage in the center of the chamber is heated up to 400 °C (calibrated to the substrate temperature, T_s) and pumped down to a low vacuum of ~10^{-1} Pa. The CBr_4 precursor (99%, Sigma-Aldrich) was vaporized at room temperature. The supply line must be continuously heated at a relatively high temperature of ~70 °C to maintain a good CBr_4 flux stability and avoid CBr_4 condensation. The CBr_4 exposure pressure was maintained at 1.3 Pa. The flow rates of Ar purging gas and H_2 reactant gas (of 99.9999% purity) were kept constant by using mass flow controllers. T_s was changed from 150 to 400 °C for assessing the effect of growth temperature on the PE-ALD growth characteristics and film properties. However, in order to study the self-limiting growth *via* saturation of the precursor exposure time (t_s), T_s was fixed at 300 °C.

2.2. Substrate pretreatments

SiO_2 layers (of 285 nm thickness) thermally grown on p-Si(100) wafers were cleaned with acetone, ethanol, and de-ionized water prior to deposition in an ultrasonic bath. Prior to the PE-ALD process, the SiO_2 substrate was hydroxylated by *in-situ* O_2 plasma pretreatment using the CCP reactor (generated power of 200 W) along with high-purity O_2 gas (99.9999%) at a fixed flow rate of 200 sccm for 30 s. The O_2 plasma pretreatment is frequently used to oxidize the surface intermediates and produce hydroxyl groups before the deposition of the subsequent layer [40]. This hydroxylation of Si by using O_2 plasma can be achieved when the oxygen plasma is contaminated with dissociated desorbed H_2O and hydrocarbons which can come from the low vacuum condition (~0.1 Pa) of the ALD chamber and the desorption and outgassing of the chamber wall with plasma surface interaction. Due to the plasma induced surface charge, the O_2 plasma treatment for a short period (tens of seconds) activates more of the —OH groups on the SiO_2 surface, which improves the subsequent adsorption with the precursor molecules [41]. The *in-situ* O_2 plasma treatment was carried out following the CBr_4 exposure pretreatment.

2.3. PE-ALD synthesis of a-C:H films

Each PE-ALD cycle consists of four sequential steps: exposure of CBr_4 to the hydroxylated SiO_2 substrate for a t_s of 4, 6, 8, 10, 14, and 18 s (step 1), purging of residual precursor molecules by inert Ar gas (step 2), exposure to hydrogen plasma gas (with a rf power of 200 W) at a partial pressure of ~10^2 Pa for a plasma pulse time (t_p) of 1.5 s (step 3), and purging of byproducts and residual H_2 reactant gas using inert Ar gas (step 4). The Ar purging gas was maintained at a fixed flow rate of 90 sccm for 8 s.

2.4. Characterization of PE-ALD a-C:H films

In order to determine the growth rates and conformality, the thickness of the deposited a-C:H film was measured using spectroscopic ellipsometry (Ellipso Technology, Elli-Se-F, λ = 380–1030 nm) and cross-sectional FE-SEM (JEOL JSM-6700F). The cross-sectional microstructure of the a-C:H film was also observed by high-resolution transmission electron microscopy (HR-TEM, Tecnai F20, FEI) with a 200 keV electron beam. For the TEM measurement, to distinguish the a-C:H film from the carbon epoxy layer, we coated a glue layer of Pt on the a-C:H film. The nanoscale surface profile of the deposited a-C:H thin film was examined by AFM (Multimode, VEECO). Raman spectroscopic measurements (Jobin Yvon, Aramis, with an Ar-ion laser excitation wavelength of 532 nm and a laser beam size of 1 μm^2) were carried out to analyze the structural arrangement of carbon atoms.

XPS measurements (ESCALab 220i-XL) of the a-C:H films were performed using a monochromatic X-ray source (Al K_α radiation, photon energy 1486.6 eV and analysis area: 100 μm^2), following surface cleaning by Ar^+ ion bombardment (energy: 3 keV; beam current density: 22.2 mA/cm^2; induced beam current: 2 mA; rastered over a

$3 \times 3\,mm^2$ area). The XPS spectra were collected in constant analyzer energy mode, at a chamber pressure of 10^{-5} Pa and pass energy of 20 eV, in steps of 0.1 eV. The deconvolution of XPS spectra was carried out with nonlinear least-square curve-fitting program (XI SDP Viewer software) with a mixed (usually 30% Gaussian) Gaussian/Lorentzian function. All spectra were referenced by setting the C 1s peak to 284.8 eV for charge correction after deconvolution. The peak area sensitivity factor method for quantitative analysis was used.

SIMS analysis was carried out at the Korean Basic Science Institute (KBSI). A SIMS equipment (CAMECA IMS-7f Auto Magnetic Sector SIMS) was utilized to detect ions (H, C, O, Si, and Br) in the carbon film with an electron neutralizer using a Cs^+ gun (impact energy: 3 keV; current: 4 nA; raster size: $200 \times 200\,\mu m^2$; analysis area: 60 μm(Φ)). The relative atomic percentage of hydrogen in the carbon film was simply calculated from the raw data of the SIMS depth profile of hydrogen and carbon which are major elements of the film.

To fabricate the C-TFT arrays, the a-C:H film was deposited onto a 285 nm-thick SiO_2 layer grown on highly doped Si substrates by using PE-ALD, as discussed above. Photolithography was used to thermally evaporate Ti (10 nm) and Au (50 nm) layers used as source and drain electrodes, respectively, on the a-C:H thin films. The reactive ion etching (RIE) process based on oxygen plasma was employed to pattern the a-C:H thin channels. Four-probe electrical measurements were carried out at ambient conditions. The gate voltage was applied through the back of the Si substrate, and the source-drain bias was fixed at 1 V.

3. Results and discussion

3.1. Effect of substrate treatment on nucleation of a-C:H by PE-ALD

Fig. 1a–d shows AFM images of a-C:H deposited by 200 PE-ALD cycles on untreated bare SiO_2, *in-situ* O_2 plasma pretreated SiO_2, and hydroxylated SiO_2 substrates with CBr_4 pre-exposure for 2 and 4 min, respectively. Fig. 1a highlights a significantly poor nucleation of carbon on the untreated bare SiO_2, whereas a larger number of carbon nuclei are observed after O_2 plasma and hydroxylation pretreatments (Fig. 1b). However, this figure shows that the hydroxylation pretreatment alone does not result in a significant enhancement of the nucleation. Thus, further pre-exposure to the CBr_4 precursor was applied prior to PE-ALD. Whereas CBr_4 pre-exposure for 2 min (Fig. 1c) is not sufficient, pre-exposure for 4 min (Fig. 1d) results in significantly increased nucleation densities, leading to a smooth carbon film with full coverage of root-mean-square (RMS) roughness of 0.36 nm. Correspondingly, as illustrated in Fig. S1 of the Supplementary Information, the Raman spectra show that the spectral intensity of the sample (Fig. 1d) deposited on the SiO_2 substrate pre-exposed to CBr_4 for 4 min is much higher than that of the sample (Fig. 1b) deposited on the hydroxylated SiO_2 substrate without CBr_4 pre-exposure.

The nucleation of deposited materials in the initial growth stage of the ALD process is strongly dependent on the properties of the substrate surface, where the chemical reaction occurs. The initial nucleation density plays a critical role in the formation of continuous films, since a high nucleation density results in a short nucleation delay time and ensures the rapid formation of a continuous layer with a smoother surface [42–44]. Indeed, various surface pretreatments, such as UV/ozone, oxygen plasma, Ar plasma, and acid treatments, can improve or alter the single-element deposition by ALD, resulting in a shorter nucleation delay time and smooth films [45–51]. Lee et al. reported that pretreating the SiO_2 surface with O_3 prior to Pt ALD increases the nucleation rate and decreases the nucleation delay time on the surface [52]. Kwon et al. demonstrated that the time required for the adsorption of the precursors to reach saturation is needed for the initial nucleation of Ru, leading to a full coverage of Ru thin films prepared by PE-ALD [53]. Also for our results of the substrate pretreatment effects

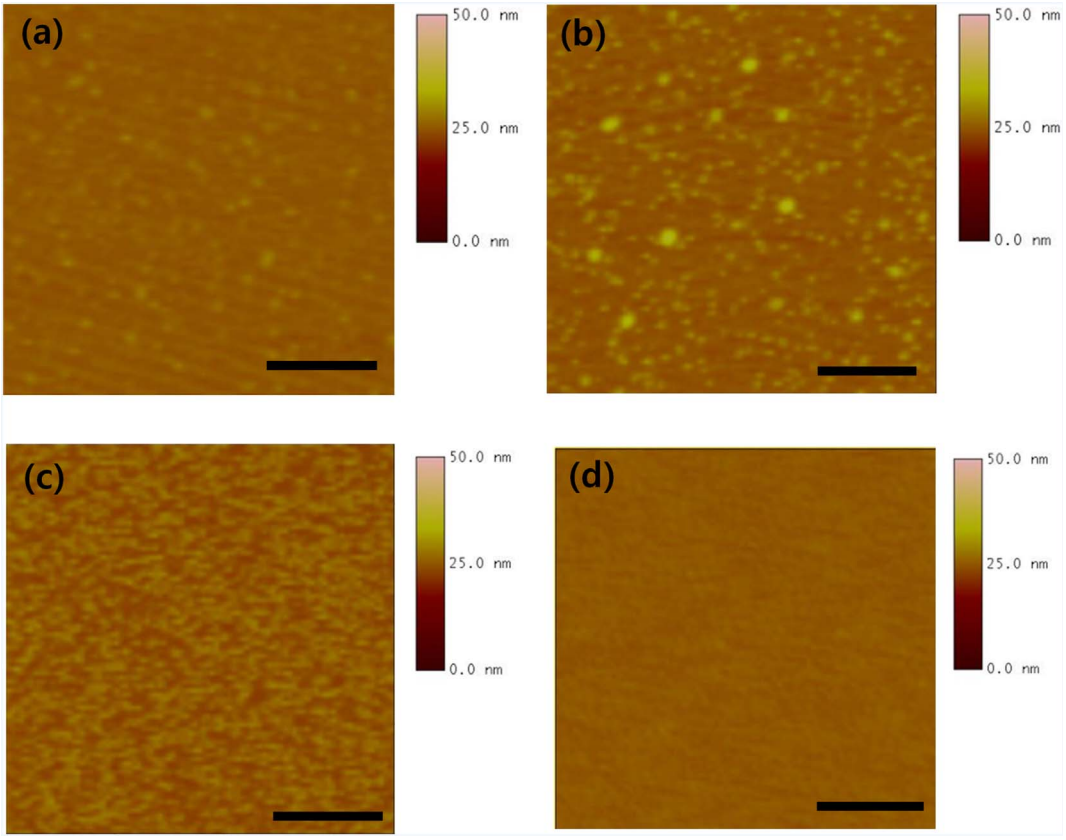

Fig. 1. AFM images of a-C:H films grown by 200 PE-ALD cycles on (a) bare SiO_2 substrate without pretreatment, (b) hydroxylated SiO_2 with *in-situ* O_2 plasma pretreatment, and (c, d) hydroxylated SiO_2 pre-exposed to CBr_4 for 2 and 4 min, respectively. The scale bars indicate 0.5 μm.

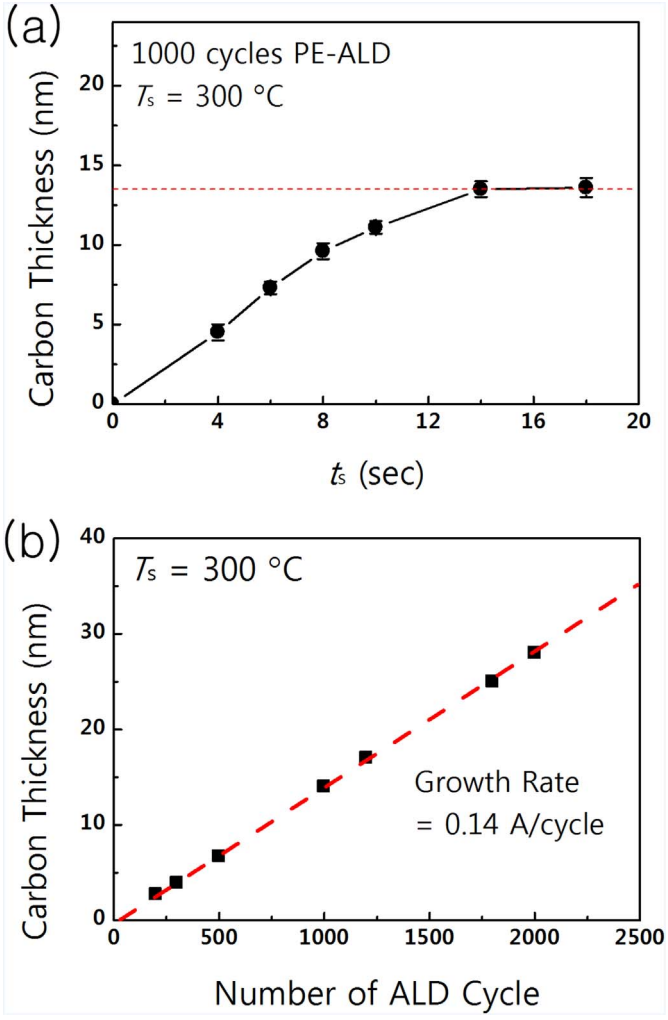

Fig. 2. Thickness of the a-C:H films deposited on SiO_2 substrates as a function of (a) the exposure time of CBr_4 precursor (t_s) and (b) the number of ALD cycles at T_s = 300 °C. The CBr_4 and H_2 plasma pulse times were 14 and 1.5 s, respectively, with 8 s purging cycles.

on the nucleation of carbon, sufficient pre-exposure to the precursor on the hydrophilic surface helps to form uniform carbon nuclei during the initial growth stage, resulting in the deposition of a smooth film.

3.2. Growth characteristics of a-C:H thin films prepared by PE-ALD

Fig. 2a shows the thickness of a-C:H films prepared by 1000 PE-ALD cycles at T_s = 300 °C, for t_s of 4, 6, 8, 10, 14, and 18 s. The thickness of the a-C:H film saturates at $t_s \geq 14$ s, indicating the self-saturation behavior in typical ALD growth mode. The saturated growth rate of the deposited a-C:H is about 0.14 Å/cycle. The thickness of the a-C:H film grown by PE-ALD at T_s = 300 °C is plotted against the number of ALD cycles in Fig. 2b, showing that the film thickness increases linearly with the number of ALD cycles. Based on these results, we fixed the precursor exposure time at t_s = 14 s in subsequent experiments. On the other hand, the Raman spectra and AFM image of the a-C:H prepared by 200 PE-ALD cycles (Fig. S2a–b in the Supplementary Information) show that increasing t_p to 3 s did not result in any improvement in the initial a-C:H film growth compared with the hydrogen plasma conditions of t_p = 1.5 s. This can be attributed to the spontaneous etching of carbon by atomic hydrogen, which leads to low growth rates [54]. The growth mechanism of a-C:H during the PE-ALD process is further discussed in Section 3.4.

Fig. 3 shows the growth rate of a-C:H PE-ALD at various T_s in a range from 150 to 400 °C. Below T_s = 200 °C, the growth rates are

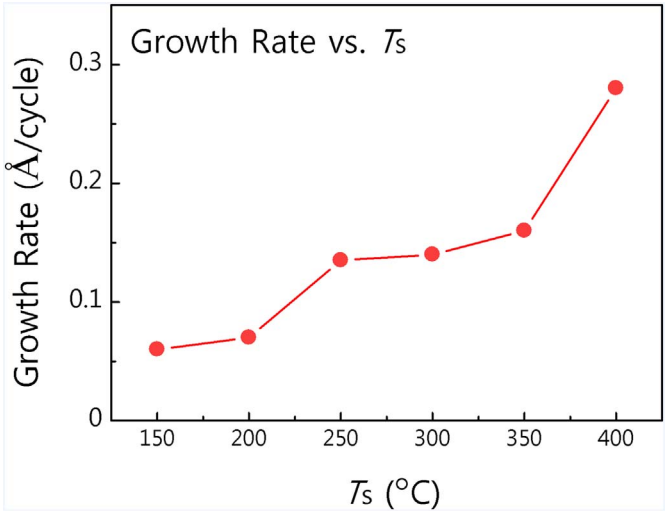

Fig. 3. Growth rates of the a-C:H films formed on a SiO_2 substrate as a function of the deposition temperature (T_s) in a range of 150–400 °C. CBr_4 and H_2 plasma pulse times were 14 and 1.5 s, respectively, with 8 s purging cycles. 2000 cycles were performed in each deposition.

under 0.07 Å/cycle, about two times lower than the 0.13–0.16 Å/cycle rates measured above T_s = 250 °C, indicating that an ALD window is the T_s in the range from 250 to 300 °C. However, since CBr_4 molecules start dissociating into reactive CBr_x ($x < 4$) at over 350 °C, the growth rate at T_s = 400 °C drastically increases by two times more than those at the ALD window. As reported in other literatures, CBr_4 exhibits high incorporation efficiency owing to its high decomposition rate on the growth surface, which in turn derives from its weak C—Br bonds [55,56]. High C doping levels in III–V group semiconductors were previously achieved by thermal decomposition of CBr_4 precursors at around 400 °C [57].

To verify the conformality of the a-C:H films obtained by the current PE-ALD process, we deposited a-C:H thin films inside *via* holes. Fig. 4 shows the cross-sectional FE-SEM image of 23 nm-thick a-C:H thin films grown in nanoscale contact hole vias with an aspect ratio of 4.5:1 (depth of 450 nm, diameter of 100 nm, and Si nitride bottom layer). The thicknesses of the a-C:H film covering all side of the *via* holes are in the

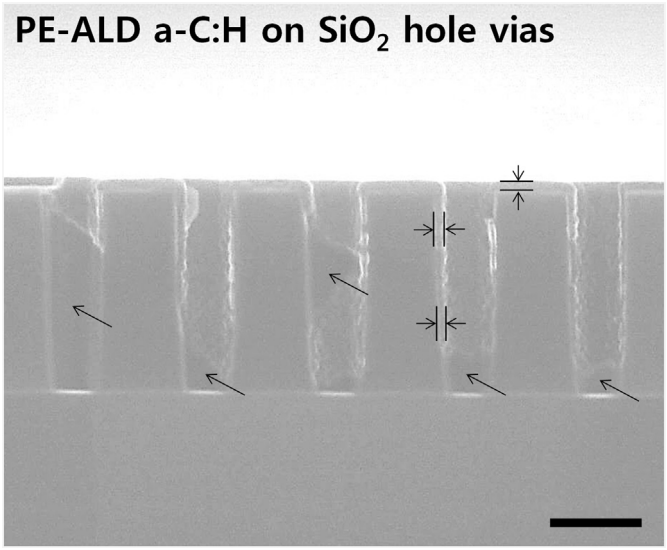

Fig. 4. Cross-sectional SEM image of the a-C:H thin films deposited by PE-ALD on SiO_2 hole vias (with aspect ratio of 4.5:1). The scale bar indicates 200 nm. The diagonal arrows indicate uncut parts of the deposited a-C:H film at the other side of hole vias during sample preparation for SEM measurements.

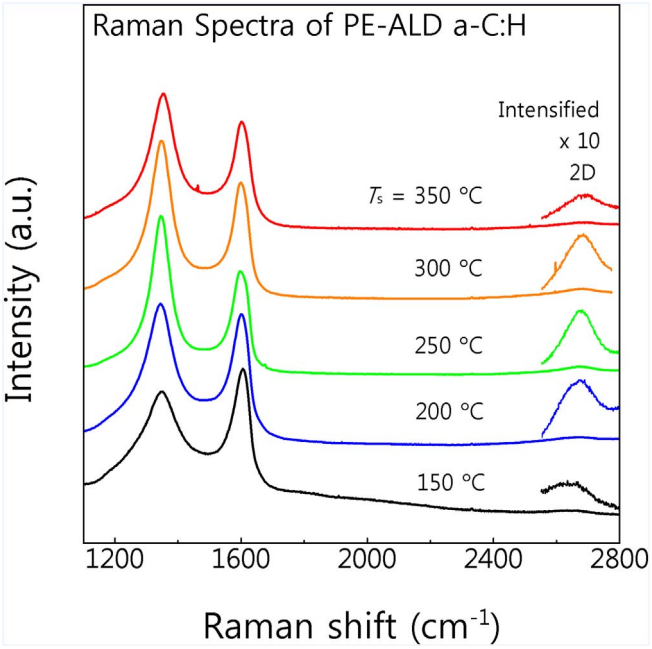

Fig. 5. Raman spectra of a-C:H films grown at T_s = 150–350 °C for 2000 ALD cycles.

21–23 nm range, confirming the good conformality of the a-C:H film prepared by PE-ALD at the ALD window. The diagonal arrow lines of the Fig. 4 indicate some uncut parts of the deposited a-C:H film at the other side of the hole vias during sample preparation for SEM measurements. However, at the higher T_s of 400 °C, thermally activated CBr_x molecules arriving directly to the substrate are likely adhere to the first solid surface that they encounter, which is resulted in low conformality coverage as shown in the supplementary Fig. S3.

3.3. Characterization of a-C:H film properties

The Raman spectra (Fig. 5) of the PE-ALD carbon films grown at T_s = 150–350 °C display three primary bands. However, the Raman spectrum (T_s = 300 °C) in the range between 1050 and 1800 cm^{-1} is deconvoluted into 7 Gaussian components after a quadratic polynomial background subtraction as shown in the supplementary Fig. S4. The 1165, 1340 and 1500 cm^{-1} peaks (blue colored) are assigned to the nanocrystalline phase of diamond, diamond and disordered sp^3 carbon, respectively. The peaks at 1360, 1585 and 1613 cm^{-1} (green colored) are assigned to the popularly known D, G and D', respectively, which are related with sp^2 hexagonal ring C clusters [58]. D, G, and 2D peaks generally correspond to disordered sp^3 C defects, in-plane bond stretching motion of pairs of C atoms in aromatic C rings or sp^2 C chains, and second-order zone boundary phonon mode, respectively. Those peaks are about 10 cm^{-1} upshifted due to an internal stress induced by film structure or other contaminants. The Raman spectra exhibit various peaks of nanocrystalline diamond and disordered sp^3 and sp^2 graphitic carbon at once, which can be attributed to a nanocrystalline sp^3 and sp^2 mixed phase and gradient film structure [59]. The Raman spectra of the carbon film grown at T_s = 150–350 °C have similar band positions of 1348 ± 5, 1600 ± 5, and 2695 ± 5 cm^{-1}, indicating that all carbon films grown by PE-ALD at those T_s have similar carbon structures. Moreover, the hydrogen content is majorly detected in the film as indicated in the SIMS depth profile (supplementary Fig. S5a). The carbon film consists of high hydrogen content-incorporated (30–45%) and disordered sp^3 polymer-like carbon at the middle and bottom side of the film and intermediate hydrogen content-incorporated (10–30%) nanocrystalline phase of diamond and aromatic hexagonal ring clusters at the top side of the film (supplementary Fig. S5b).

In order to examine the crystal structures of the a-C:H film using TEM, we deposited a 28 nm-thick a-C:H film grown by 2000 PE-ALD cycles onto a SiO_2 substrate at T_s = 300 °C. We can distinguish the PE-ALD a-C:H film with high contrast from the black Pt glue which has been used by the sample preparation for HR-TEM measurements. Fig. 6a shows the cross-sectional TEM image of the Pt glue layer/PE-ALD a-C:H/SiO_2 film structure. The HR-TEM image (Fig. 6b), which shows a magnified view of the area marked by the yellow box in Fig. 6a, highlights the nanocrystalline sp^2 and sp^3 carbon lattices of the a-C:H film and other amorphous phase of the bottom layer. During the wedge polishing, Pt glue was pushed into the polished interface.

Fig. 7 shows the XPS spectra of the a-C:H film grown by 2000 PE-ALD cycles at T_s = 200 and 300 °C. The C 1s spectra (Fig. 7a) can be fitted by six Gaussian/Lorentzian (mixed usually 30% Gaussian) components, with binding energies of 284.6 eV (sp^2 graphitic carbon), 285.3 eV (C—C), 286.1 eV (C—O and C—Br), 287.1 eV (C═O groups), 288.4 eV (OCO groups), and 290.2 (—COO groups). The Br 3p spectra (Fig. 7b) consist of two peaks at 183.2 and 190.1 eV, denoting the presence of bromine residues in the a-C:H films. The atomic percentage of carbon, oxygen, and bromine elements in the a-C:H films is shown in Fig. 7c. As T_s increases from 200 to 300 °C, the oxygen content in the a-C:H film decreases from 17.0 to 9.1 at.% and the carbon content increases from 81.1 to 90.5 at.%, which are in good agreement with the contents found in a-C:H films deposited by other techniques [60,61]. These oxygen species may originate from the incorporation of oxygen in

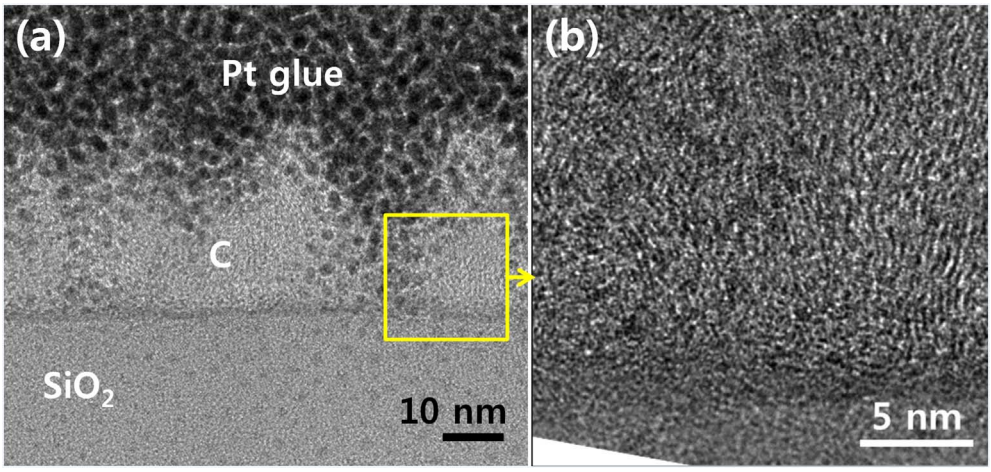

Fig. 6. (a) Cross-sectional TEM image of the PE-ALD a-C:H film (T_s = 300 °C) on a SiO_2/Si substrate with Pt glue layer. (b) HR-TEM magnified image of the area within the yellow box in panel (a). (For interpretation of the references to color in this figure legend, the reader is referred to the web version of this article.)

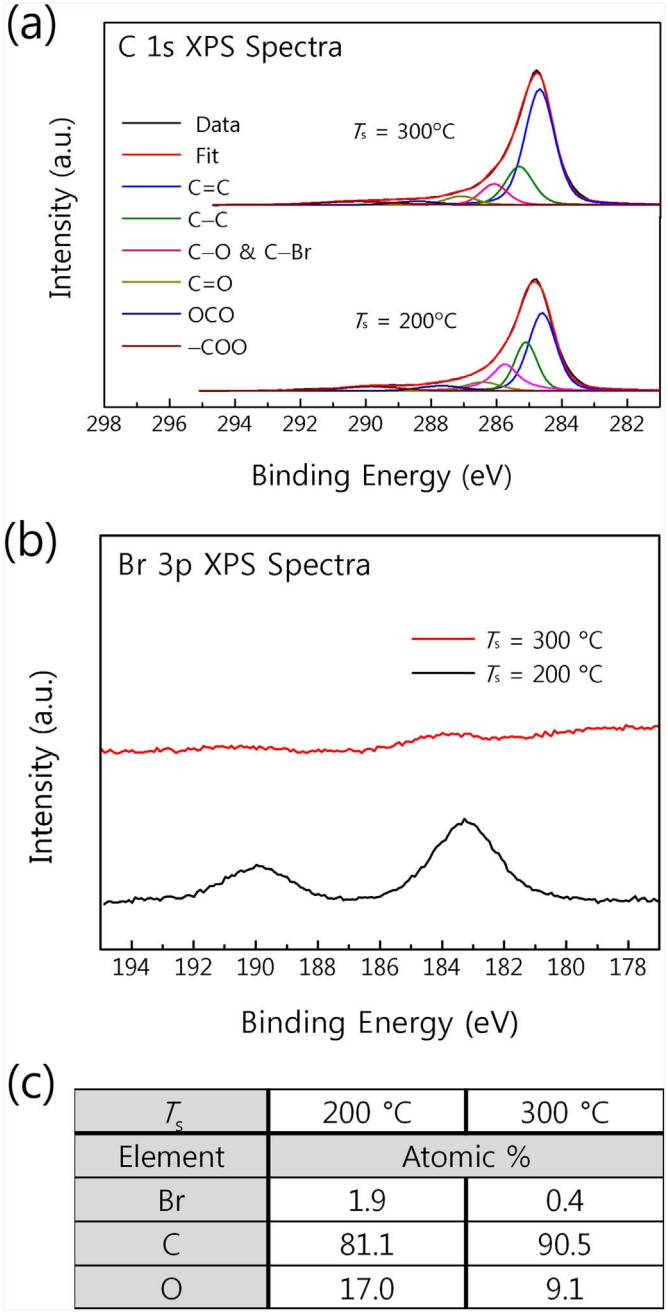

(c)

T_s	200 °C	300 °C
Element	Atomic %	
Br	1.9	0.4
C	81.1	90.5
O	17.0	9.1

Fig. 7. XPS spectra of C 1s (a) and Br 3p (b) core levels of the a-C:H films grown by PE-ALD on hydroxylated SiO_2 substrates at T_s = 200 and 300 °C. (c) Elemental atomic percentages in those a-C:H films.

the amorphous film structures after deposition, since *ex-situ* measurements were performed after prolonged air exposure. The larger portion of C—C, C—O, C—Br, and C═O peak in the XPS C 1s spectra at T_s = 200 than that of T_s = 300 °C can be attributed to the increase of the covalent bonds with oxygen and bromine species and the disordered sp^3 carbon defects. Whereas, the bromine level in the a-C:H film significantly decreases from 1.9 to 0.4 at.%, indicating that the Br ligands of the CBr_4 precursor molecules react thoroughly with atomic hydrogen, forming HBr byproduct molecules purged in each PE-ALD cycle, and that the quality of the a-C:H films depends on T_s, according to the degree of oxygen incorporation.

The bonding characteristics of the a-C:H films were further analyzed by FT-IR spectroscopy, as shown in Fig. 8. Several peaks of different intensities are visible in the FT-IR spectra, which were baseline-

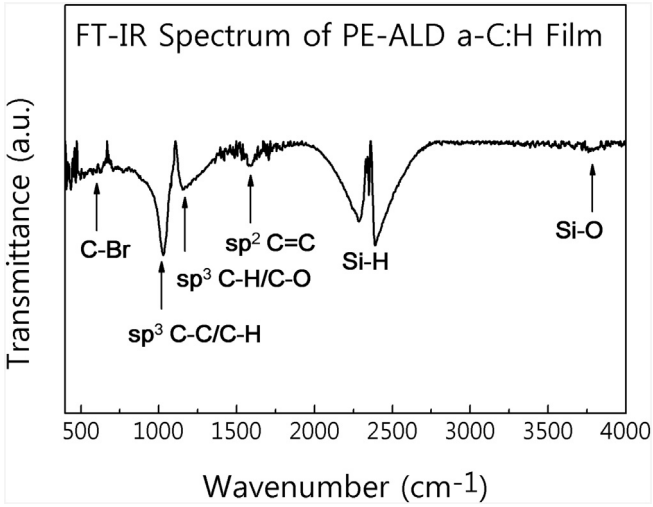

Fig. 8. FT-IR spectrum of the a-C:H film grown by PE-ALD at T_s = 300 °C.

corrected using the FT-IR spectrum of a SiO_2/Si substrate. The strong absorption peak at 1037 cm^{-1} is assigned to the sp^3 C—C stretching/C—H bending vibrations, and the broad band at around 1105–1375 cm^{-1} is attributed to the sp^3 C—H/C—O stretching modes [62]. The weak absorption peak at 1614 cm^{-1} corresponds to the stretching vibration of sp^2 C═C bonds, whereas the C—Br stretching gives rise to a weak and broad absorption band around 500–800 cm^{-1} [63,64]. These results indicate that the present PE-ALD-grown a-C:H films consist of low level oxygen- and bromine-incorporated and hydrogenated nanocrystalline sp^3 carbon and non-hydrogenated sp^2 carbon. Hydrogen radicals play a role not only in the hydrogenation of carbon film but also in extraction of Br ligands and etching of C atoms in the sequential exposure manner during PE-ALD process, which is to be discussed in the Section 3.4.

The sheet resistance (R_{sh}) and resistivity (ρ) were obtained by the measurements using a four-point probe technique (Table 1), as these values are inversely proportional to the conductivity and closely related to the film quality and graphitic C components of the a-C:H film. The a-C:H film grown at T_s = 300 °C shows R_{sh} of 88 kΩ/sq and ρ of 0.25 Ω·cm, which is much lower than that of the a-C:H film grown at T_s = 200 °C, indicating that the electrical resistivity of the PE-ALD a-C:H film become lower as the T_s increases. Thus, we further evaluated the semiconducting properties of the a-C:H thin films deposited at T_s = 200 and 300 °C, by fabricating the C-TFTs illustrated in Fig. 9a. Fig. 9b shows the representative I_{DS}-V_G transfer curve (where I_{DS} is the source-drain current and V_G is the gate voltage) of the C-TFTs. The gate voltage was swept from −100 to +100 V with a step size of 0.5 V. The I_{DS} value decreased with increasing gate voltage under a fixed V_{DS} of 1 V (where V_{DS} is the source-drain voltage), showing that the present a-C:H films behave as weak p-type semiconductors under ambient conditions. Most of the a-C including undoped a-C, diamond-like carbon, and nanocrystalline graphitic carbon are already proved to be weak p-type semiconductors [1,7]. The field-effect mobility was estimated from the $\Delta I_{DS}/\Delta V_G$ slope, which was fitted to the linear regime of the transfer curves according to the equation $\mu_{eff} = (\Delta I_{DS}/\Delta V_G)(1/(V_{DS}C_{OX})L/W)$,

Table 1
Electrical properties of the a-C:H films grown at T_s = 200 and 300 °C compared with other literatures.

Electrical property	200 °C PE-ALD a-C:H	300 °C PE-ALD a-C:H	Other literatures [65–68]
R_{sh} (kΩ/□)	1155	88	3.4–110
μ_{eff} ($cm^2 V^{-1} s^{-1}$)	0.1	1.7	1–5
ρ (Ω)	1.62	0.25	0.005–0.42

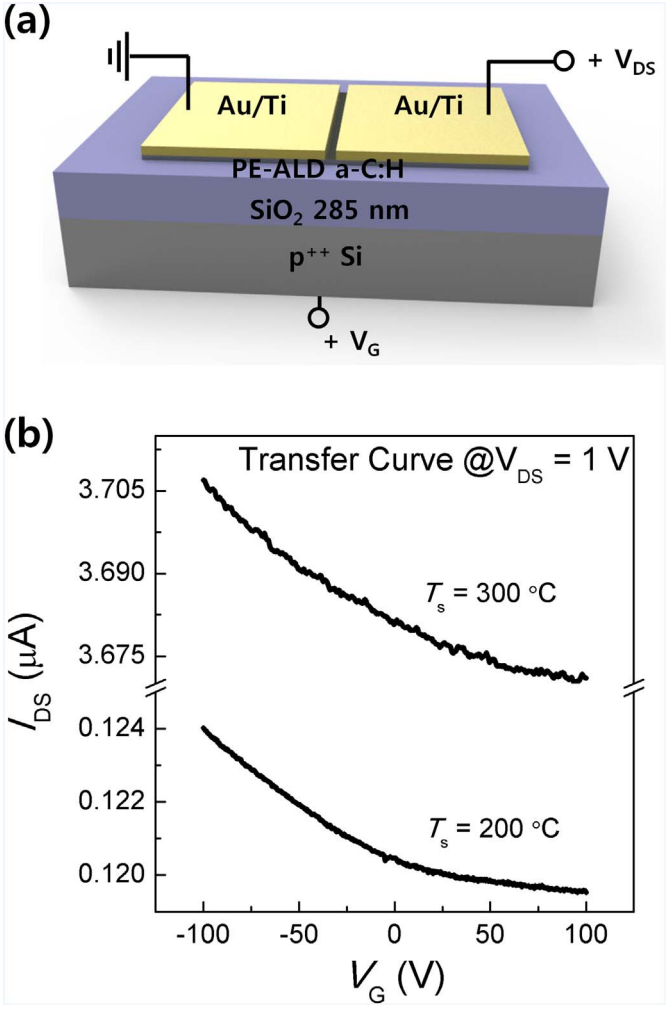

Fig. 9. (a) Schematic illustration of C-TFT with Au/Ti source and drain electrodes, and a SiO_2 gate dielectric film. (b) Transfer curves of C-TFTs with a-C:H thin film channels grown at T_s = 200 and 300 °C. All measurements were carried out at V_{DS} = 1 V in room temperature ambient air.

where L (14 μm) and W (7 μm) are the channel length and width, respectively, and C_{OX} is the gate oxide (a 285 nm-thick SiO_2 layer) capacitance per unit area, which was measured as 4 nF/cm^2. The a-C:H film grown at T_s = 300 °C has a mobility of 1.7 cm^2 V^{-1} s^{-1}, which is comparable to the previously reported mobility of carbon TFTs [65–68]. On the other hand, the mobility of the a-C:H film grown at T_s = 200 °C is one order of magnitude lower than that of the a-C:H film grown at T_s = 300 °C. This decrease in mobility is attributed to the T_s-dependent properties of the a-C:H film, such as the purity and low defect density of the a-C:H film, which are expected to significantly decrease as T_s decreases from 300 to 200 °C (as highlighted by the XPS results shown in Fig. 7).

3.4. Growth mechanism of a-C:H films grown by PE-ALD on the hydroxylated SiO_2 substrate

Some insight into the growth mechanism of the films can be obtained from previous investigations of the gas-phase alkyl halide chemistry and of the surface chemistry of hydroxylated Si substrates. These studies highlighted the surface chemical reaction of halide (fluoride, chloride, bromide, and iodide) molecules on a hydroxylated Si substrate, along with the charge transfer between surface hydroxyl groups and the halogen ligands [39,69,70]. It has been reported that, for chloride precursors dissociatively adsorbed on the hydroxylated SiO_2 substrates, the surface hydroxyl groups act as adsorption sites for $TiCl_4$, $HfCl_4$, and $ZrCl_4$ precursor molecules in the initial stages of the ALD of TiN, HfO_2, and ZrO_2 films, respectively [44,49,71]. In the present case, during the first half-cycle chemical reaction that takes place in the initial step of the PE-ALD of a-C:H films, the surface reaction of CBr_4 precursor molecules on the active sites of a hydroxylated SiO_2 surface may occur as indicated below:

$$OH(s) + CBr_4(g) = O - CBr_3(ads) + H - Br(g), \quad (1)$$

where (s) denotes the surface species; (g) is the gas phase; (ads) is the adsorbed species. Because the generated HBr byproduct can be removed by the inert gas, the surface chemical reaction can be assumed irreversible and rate limiting [72]. According to this scheme, during CBr_4 exposure in a PE-ALD cycle, the reactive CBr_3 species are chemisorbed on the SiO_2 surface. The second half-cycle would involve exposure to atomic H originating from plasma, and a purging period separates subsequent half-cycles:

$$O - CBr_3(ads) + H(g) \rightarrow O - CBr_2(s) + H - Br(g) \quad (2a)$$

$$O - CBr_2(ads) + H(g) \rightarrow O - CBr(s) + H - Br(g) \quad (2b)$$

$$O - CBr(ads) + H(g) \rightarrow O - C(s) + H - Br(g) \quad (2c)$$

The atomic hydrogen fluxes impinging on the surface extract some of the Br species, producing CBr_2 and CBr groups and allowing further chemical reaction producing HBr byproduct molecules and C—H species, while desorption of HBr can also occur. The driving force to this reaction, and many similar ALD reactions involving halogen precursors, is the extraction of Br atoms from CBr_4 by atomic H, to form volatile HBr. For a subsequent ALD cycle, new CBr_4 precursors react with the C—H or defective sp^3 C species of an initial C layer which have been formed in the previous second half-cycle. After the precursor purging and reactant exposing and purging steps, new C adatoms or C—H species are deposited and play an active role in the next reaction.

Previous studies have shown that the Eley-Rideal (ER) surface kinetics, in addition to the conventional Langmuir-Hinshelwood (LH) kinetics, play an important role in the Br extraction from the Si surface by atomic H [73,74]. In the case of the ER mechanism, the extraction reaction occurs directly as soon as the reagents hit the adsorbent, while in the LH mechanism the reaction takes places between reagents that are chemisorbed and in thermal equilibrium. In other words, the driving force for Br extraction is represented by the high internal energy of atomic hydrogen. One of the characteristics of the ER mechanism is the relatively small activation energy of the extraction reaction. According to our experimental results, an increase in the growth temperature from 200 to 300 °C led to growth rates increasing by a factor of 2 and atomic percentages of Br in the a-C:H films decreasing by a factor of 5. Although the Br extraction rate can be somewhat accelerated by raising the substrate temperature, the growth rate is significantly small, around 0.1 Å/cycle, because the reaction is driven mainly by the high internal energy of atomic hydrogen, rather than by the thermal energy of the substrate. Moreover, it has been reported that the carbon film surfaces exposed to a flux of atomic hydrogen are chemically eroded *via* hydrocarbon production at around 400–700 K, with an erosion efficiency of 0.01C atoms per incoming H [54]. As shown in Fig. S2a–b (Supplementary Information) and discussed in Section 3.2, the Raman intensity and nucleation density of the deposited a-C:H decrease with increasing hydrogen plasma pulse time in the initial PE-ALD cycles, indicating that the initial growth of a-C:H is significantly affected by the hydrogen plasma. Although the etching of the carbon surface by atomic hydrogen attributes the growth rates to decrease, hydrogen plasma radicals play a major role in the formation of a-C:H on the hydroxylated substrate. Firstly, small a-C nuclei are formed on the hydroxylated SiO_2 by initial PE-ALD process and a partial formation of dangling bonds on the a-C nucleus occurs due to a cause in the formation of nucleation sites by atomic hydrogen exposure. Secondly, adsorbed CBr_x on

nucleation sites condenses to form a-C:H islands with dangling bonds after the subsequent PE-ALD cycles. Thirdly, nucleated a-C:H on the edges or defect sites of a-C:H islands with dangling bonds occurs prior to two dimensional growth and the subsequent formation of a-C:H film with random orientation during continuous PE-ALD cycles. Lastly, reactive carbon species arriving at the edges or defect sites of the nucleated a-C:H film with random orientations are easily bonded to the neighbored edges or defects and eventually the a-C:H film expands preferably along the direction of atomic hydrogen radical diffusion (vertical flow direction in the CCP reactor). In that initial nucleation step, randomly oriented hydrocarbon species and relatively excessive hydrogen content in the hydrogen plasma can lead to a large amount of hydrogen bonded or trapped into the a-C:H film. This can be responsible for the soft and porous polymer-like carbon structure of the bottom layer. Continuously, under the high plasma energy during the reactant exposure step, the combined ion bombardment and thermal effects may result in the effusion of weakly bonded hydrogen atoms and formation of the aromatic sp^2 hexagonal ring structures caused by an increased connectivity of sp^2 carbon sites [75].

4. Conclusions

In conclusion, a-C:H thin films were grown by PE-ALD at low growth temperatures in the range of 150–350 °C using CBr_4 precursor and H_2 plasma reactants. According to Raman, SIMS, FT-IR, and XPS results, the carbon films contained hydrogenated nanocrystalline sp^3 diamond and sp^2 graphitic carbons, and disordered sp^3 carbon defects incorporated with oxygen and bromine. The growth rate at 300 °C was found to saturate at ~0.14 Å/cycle with respect to the exposure time to the CBr_4 precursor. Substrate pretreatments by plasma hydroxylation and precursor exposure are helpful for the uniform nucleation of carbon. It was also shown that PE-ALD-grown a-C:H films can be deposited on three-dimensional structures in a conformal manner. The electrical properties of the a-C:H films were found to be comparable with those reported for other a-C films deposited by high-temperature CVD. This newly developed low-temperature PE-ALD of a-C:H can be employed as a conformal carbon nano-coating process on three-dimensional nanostructures.

Acknowledgements

This work was supported by a National Research Foundation of Korea (NRF) grant funded by the Korea government (MSIP) (Grant No. NRF-2017R1C1B5076821). In addition, this work was supported by the Center for Integrated Smart Sensors funded by the Ministry of Science, ICT & Future Planning as Global Frontier Project (Project No. CISS-2016M3A6A6930869).

Appendix A. Supplementary data

Supplementary data to this article can be found online at https://doi.org/10.1016/j.surfcoat.2018.02.082.

References

[1] J. Robertson, Diamond-like amorphous carbon, Mater. Sci. Eng. R. Rep. 37 (2002) 129–281.
[2] M.J. Allen, V.C. Tung, R.B. Kaner, Honeycomb carbon: a review of graphene, Chem. Rev. 110 (2010) 132–145.
[3] G. Galli, R.M. Martin, R. Car, M. Parrinello, Structural and electronic properties of amorphous carbon, Phys. Rev. Lett. 62 (1989) 555–558.
[4] X. Fan, Q. Xue, L. Wang, Carbon-based solid–liquid lubricating coatings for space applications – a review, Friction 3 (2015) 191–207.
[5] F. Legrain, J. Sottmann, K. Kotsis, S. Gorantla, S. Sartori, S. Manzhos, Amorphous (glassy) carbon, a promising material for sodium ion battery anodes: a combined first-principles and experimental study, J. Phys. Chem. C 119 (2015) 13496–13501.
[6] T. Lee, N.K. Min, H.W. Lee, J. Jang, D. Lee, M. Hong, et al., The deposition of amorphous carbon thin films for hard mask applications by reactive particle beam assisted sputtering process, Thin Solid Films 517 (2009) 3999–4002.
[7] R. Ur, R. Sagar, X. Zhang, C. Xiong, Y. Yu, Semiconducting amorphous carbon thin films for transparent conducting electrodes, Carbon 76 (2014) 64–70.
[8] J.D. Wilcox, M.M. Doeff, M. Marcinek, R. Kostecki, Factors influencing the quality of carbon coatings on $LiFePO_4$, J. Electrochem. Soc. 154 (2007) A389–A395.
[9] S. Kim, D. Padhi, S.H. Hong, B.H. Kim, D.R. Witty, Conformal amorphous carbon for spacer and spacer protection applications, US Pat. 0279676 (2015).
[10] H. Li, H. Zhou, Enhancing the performances of Li-ion batteries by carbon-coating: present and future, Chem. Commun. 48 (2012) 1201–1217.
[11] D.W.M. Lau, A. Moafi, M.B. Taylor, J.G. Partridge, D.G. McCulloch, R.C. Powles, et al., The structural phases of non-crystalline carbon prepared by physical vapour deposition, Carbon 47 (2009) 3263–3270.
[12] Y. Pauleau, F. Thièry, V.V. Uglov, V.M. Anishchik, A.K. Kuleshov, M.P. Samtsov, Tribological properties of copper/carbon films formed by microwave plasma-assisted deposition techniques, Surf. Coat. Technol. 180–181 (2004) 102–107.
[13] A.C. Ferrari, B. Kleinsorge, N.A. Morrison, A. Hart, V. Stolojan, J. Robertson, Stress reduction and bond stability during thermal annealing of tetrahedral amorphous carbon, J. Appl. Phys. 85 (1999) 7191–7197.
[14] A.M. Bonnot, M. Deldem, E. Beaugnon, T. Fournier, M.C. Schouler, M. Mermoux, Carbon nanostructures and diamond growth by HFCVD: role of the substrate preparation and synthesis conditions, Diam. Relat. Mater. 8 (1999) 631–635.
[15] P.S. Banks, L. Dinh, B.C. Stuart, M.D. Feit, A.M. Komashko, A.M. Rubenchik, et al., Short-pulse laser deposition of diamond-like carbon thin films, Appl. Phys. A Mater. Sci. Process. 69 (1999) S347–S353.
[16] X.B. Yan, T. Xu, S.R. Yang, H.W. Liu, Q.J. Xue, Characterization of hydrogenated diamond-like carbon films electrochemically deposited on a silicon substrate, J. Phys. D. Appl. Phys. 37 (2004) 2416–2424.
[17] H. Kim, H.B.R. Lee, W.J. Maeng, Applications of atomic layer deposition to nanofabrication and emerging nanodevices, Thin Solid Films 517 (2009) 2563–2580.
[18] J. Lu, J.W. Elam, P.C. Stair, Atomic layer deposition — sequential self-limiting surface reactions for advanced catalyst "bottom-up" synthesis, Surf. Sci. Rep. 71 (2016) 410–472.
[19] H. Kim, Atomic layer deposition of metal and nitride thin films: current research efforts and applications for semiconductor device processing, J. Vac. Sci. Technol. B 21 (2003) 2231–2261.
[20] T. Hukka, R. Rawles, M. Develyn, Novel method for chemical vapor-deposition and atomic layer epitaxy using radical chemistry, Thin Solid Films 225 (1993) 212–218.
[21] S.F. Komarov, J.-J. Lee, J.B. Hudson, M.P. D'Evelyn, Self-limiting diamond growth from alternating CF_x and H fluxes, Diam. Relat. Mater. 7 (1998) 1087–1094.
[22] Y. Zhang, W. Ren, Z. Jiang, S. Yang, W. Jing, P. Shi, X. Wu, Z. Ye, Low-temperature remote plasma-enhanced atomic layer deposition of graphene and characterization of its atomic-level structure, J. Mater. Chem. C 2 (2014) 7570–7574.
[23] J. Hämäläinen, M. Ritala, M. Leskelä, Atomic layer deposition of noble metals and their oxides, Chem. Mater. 26 (2014) 786–801.
[24] H. Kim, I.-K. Oh, Review of plasma-enhanced atomic layer deposition: technical enabler of nanoscale device fabrication atomic layer deposition, Jpn. J. Appl. Phys. 53 (2014) 03DA01.
[25] S. Sugahara, Y. Uchida, T. Kitamura, T. Nagai, M. Matsuyama, T. Hattori, et al., A proposed atomic-layer-deposition of germanium on Si surface, Jpn. J. Appl. Phys. Part 1 Regul. Pap. Short Notes Rev. Pap. 36 (1997) 1609–1613.
[26] D.D. Koleske, S.M. Gates, Atomic layer epitaxy of Si on Ge(100) using Si_2Cl_6 and atomic hydrogen, Appl. Phys. Lett. 64 (1994) 884–886.
[27] H. Kim, S.M. Rossnagel, Growth kinetics and initial stage growth during plasma-enhanced Ti atomic layer deposition, J. Vac. Sci. Technol. A 20 (2002) 802–808.
[28] D.-Y. Moon, W.-S. Kim, T.-S. Kim, B.-W. Kang, J.-W. Park, S.J. Yeom, et al., Atomic layer deposition of copper seed layers from a (hfac)Cu(VTMOS) precursor, J. Korean Phys. Soc. 54 (2009) 1330–1333.
[29] H. Kim, S.M. Rossnagel, Plasma-enhanced atomic layer deposition of tantalum thin films: the growth and film properties, Thin Solid Films 441 (2003) 311–316.
[30] M. Kariniemi, J. Niinistö, T. Hatanpää, M. Kemell, T. Sajavaara, M. Ritala, et al., Plasma-enhanced atomic layer deposition of silver thin films, Chem. Mater. 23 (2011) 2901–2907.
[31] N.E. Lay, G.A. Ten Eyck, D.J. Duquette, T.-M. Lu, Direct plating of cu on Pd plasma enhanced atomic layer deposition coated TaN barrier, Electrochem. Solid-State Lett. 10 (2007) D13–D16.
[32] S.J. Paddison, E. Tschuikow-Roux, Structures, vibrational frequencies, thermodynamic properties, and bond dissociation energies of the bromomethanes and bromomethyl radicals: an ab initio study, J. Phys. Chem. A 102 (1998) 6191–6199.
[33] C.F. Matta, N. Castillo, R.J. Boyd, Atomic contributions to bond dissociation energies in aliphatic hydrocarbons, J. Chem. Phys. 125 (2006) 204103.
[34] J.V. Michael, K.P. Lim, S.S. Kumaran, J.H. Kiefer, Thermal decomposition of carbon tetrachloride, J. Phys. Chem. 97 (1993) 1914–1919.
[35] Y.J. Kime, D.C. Driscoll, P.A. Dowben, The stability of the carbon tetrahalide ions, J. Chem. Soc. Faraday Trans. 2 (83) (1987) 403–410.
[36] Q.F. Huang, S.F. Yoon, K.H. Tan, Z.Z. Sun, R. Zhang, J. Jiang, et al., Carbon doping in GaAs using carbon tetrabromide in solid source molecular beam epitaxy, J. Cryst. Growth 252 (2003) 37–43.
[37] K. Tateno, Y. Kohama, C. Amano, Carbon doping and etching effects of CBr4 during metalorganic chemical vapor deposition of GaAs and AlAs, J. Cryst. Growth 172 (1997) 5–12.
[38] T.J. de Lyon, N.I. Buchan, P.D. Kirchner, J.M. Woodall, G.J. Scilla, F. Cardone, High carbon doping efficiency of bromomethanes in gas source molecular beam epitaxial growth of GaAs, Appl. Phys. Lett. 58 (1991) 517–519.
[39] X.J. Zhou, Q. Li, Z.H. He, X. Yang, K.T. Leung, Dissociative adsorption and thermal desorption of dibromoethylene on Si(100)2 × 1: surface mediated dehalogenation and recombinative evolution of HBr, Surf. Sci. 543 (2003) L668–L674.
[40] T. Suni, K. Henttinen, I. Suni, J. Mäkinen, Effects of plasma activation on

hydrophilic bonding of Si, J. Electrochem. Soc. 149 (2002) G348–G351.
[41] X. Zhang, J.-P. Raskin, Low-temperature wafer bonding optimal O_2 plasma surface pretreatment time, Electrochem. Solid-State Lett. 7 (2004) G172–G174.
[42] J.W. Elam, C.E. Nelson, R.K. Grubbs, S.M. George, Nucleation and growth during tungsten atomic layer deposition on SiO_2 surfaces, Thin Solid Films 386 (2001) 41–52.
[43] H.-B.-R. Lee, Y.J. Park, S. Baik, H. Kim, Initial stage growth during plasma-enhanced atomic layer deposition of cobalt, Chem. Vap. Depos. 18 (2012) 41–45.
[44] J.J. Pyeon, C.J. Cho, S.H. Baek, C.Y. Kang, J.S. Kim, D.S. Jeong, et al., Control of the initial growth in atomic layer deposition of Pt films by surface pretreatment, Nanotechnology 26 (2015) 304003.
[45] J. Heo, S.-J. Won, D. Eom, S.Y. Lee, Y.B. Ahn, C.S. Hwang, et al., The role of the methyl and hydroxyl groups of low-k dielectric films on the nucleation of ruthenium by ALD, Electrochem. Solid-State Lett. 11 (2008) H210–H213.
[46] A. Satta, M. Baklanov, O. Richard, A. Vantomme, H. Bender, T. Conard, et al., Enhancement of ALCVD™ TiN growth on Si–O–C and α-SiC:H films by O_2-based plasma treatments, Microelectron. Eng. 60 (2002) 59–69.
[47] C. Liu, C.-C. Wang, C.-C. Kei, Y.-C. Hsueh, T.-P. Perng, Atomic layer deposition of platinum nanoparticles on carbon nanotubes for application in proton-exchange membrane fuel cells, Small 5 (2009) 1535–1538.
[48] M.J. Weber, A.J.M. Mackus, M.A. Verheijen, V. Longo, A.A. Bol, W.M.M. Kessels, Atomic layer deposition of high-purity palladium films from $Pd(hfac)_2$ and H_2 and O_2 plasmas, J. Phys. Chem. C 118 (2014) 8702–8711.
[49] Y.-C. Hsueh, C.-T. Hu, C.-C. Wang, C. Liu, T.-P. Perng, Deposition of Pt nanoparticles on oxygen plasma treated carbon nanotubes by atomic layer deposition, ECS Trans. 16 (2008) 855–862.
[50] J. Li, J. Wu, C. Zhou, B. Han, E.J. Karwacki, M. Xiao, et al., On the dissociative chemisorption of tris(dimethylamino)silane on hydroxylated SiO_2(001) surface, J. Phys. Chem. C 113 (2009) 9731–9736.
[51] L. Jeloaica, A. Estève, M.D. Rouhani, D. Estève, Density functional theory study of $HfCl_4$, $ZrCl_4$, and $Al(CH_3)_3$ decomposition on hydroxylated SiO_2: initial stage of high-k atomic layer deposition, Appl. Phys. Lett. 83 (2003) 542–544.
[52] H.-B.-R. Lee, K.L. Pickrahn, S.F. Bent, Effect of O_3 on growth of Pt by atomic layer deposition, J. Phys. Chem. C 118 (2014) 12325–12332.
[53] S.-H. Kwon, O.-K. Kwon, J.-H. Kim, H.-R. Oh, K.-H. Kim, S.-W. Kang, Initial stages of ruthenium film growth in plasma-enhanced atomic layer deposition, J. Electrochem. Soc. 155 (2008) H296–H300.
[54] A. Horn, A. Schenk, J. Biener, B. Winter, C. Lutterloh, M. Wittmann, et al., H atom impact induced chemical erosion reaction at C:H film surfaces, Chem. Phys. Lett. 231 (1994) 193–198.
[55] T. Choi, S.H. Kim, C.W. Lee, H. Kim, S.-K. Choi, S.-H. Kim, et al., Synthesis of carbon nanotube-nickel nanocomposites using atomic layer deposition for high-performance non-enzymatic glucose sensing, Biosens. Bioelectron. 63 (2015) 325–330.
[56] T. Choi, H. Jung, C.W. Lee, K.Y. Mun, S.H. Kim, J. Park, et al., Growth characteristics of graphene synthesized via chemical vapor deposition using carbon tetrabromide precursor, Appl. Surf. Sci. 343 (2015) 128–132.
[57] H. Ito, S. Yamahata, N. Shigekawa, K. Kurishima, Y. Matsuoka, High-speed carbon-doped-base InP/InGaAs heterojunction bipolar transistors grown by MOCVD, Electron. Lett. 31 (1995) 2128–2130.
[58] P.K. Chu, L. Li, Characterization of amorphous and nanocrystalline carbon films, Mater. Chem. Phys. 96 (2006) 253–277.
[59] S. Neuville, Carbon Structure Analysis with Differentiated Raman Spectroscopy, Lambert Academic Publishing Eds, 2014 (ISBN 978-3-659-48909-9).
[60] D. Pradhan, M. Sharon, Opto-electrical properties of amorphous carbon thin film deposited from natural precursor camphor, Appl. Surf. Sci. 253 (2007) 7004–7010.
[61] J. Filik, P.W. May, S.R.J. Pearce, R.K. Wild, K.R. Hallam, XPS and laser Raman analysis of hydrogenated amorphous carbon films, Diam. Relat. Mater. 12 (2003) 974–978.
[62] R.N. Tiwari, J.N. Tiwari, L. Chang, M. Yoshimura, Enhanced nucleation and growth of diamond film on Si by CVD using a chemical precursor, J. Phys. Chem. C 115 (2011) 16063–16073.
[63] P.A. Troshin, E. Kemnitz, S.I. Troyanov, Characterization of reactions of fullerene C60 with bromine. Crystal structures of bromofullerenes, Russ. Chem. Bull. 53 (2004) 2787–2792.
[64] S. Singhal, C. Singh, P. Singla, K. Dharamvir, Effect of magnetic field on the growth of aligned carbon nanotubes using a metal free arc discharge method and their purification, Solid State Phenom. 201 (2013) 197–209.
[65] M. Schreiber, T. Lutz, G.P. Keeley, S. Kumar, M. Boese, S. Krishnamurthy, et al., Transparent ultrathin conducting carbon films, Appl. Surf. Sci. 256 (2010) 6186–6190.
[66] C.-C. Liu, A.B. Walters, M.A. Vannice, Measurement of electrical properties of a carbon black, Carbon 33 (1995) 1699–1708.
[67] R. Ur Rehman, X. Zhang Sagar, J. Wang, C. Xiong, Negative magnetoresistance in undoped semiconducting amorphous carbon films, J. Appl. Phys. 115 (2014) 123708.
[68] H. Kinoshita, M. Kubota, G. Ohno, Deposition of amorphous carbon films using Ar and/or N_2 magnetron sputter with ring permanent magnet, Thin Solid Films 523 (2012) 52–54.
[69] A.A. Chuiko, Chemistry of silica surfaces and mechanisms of chemical reactions, Bull. Acad. Sci. USSR, Div. Chem. Sci. 39 (1990) 2173–2184.
[70] F.H. Van Cauwelaert, J.B. Van Assche, J.B. Uytterhoeven, Adsorption of methyl bromide on the surface hydroxyls of silica gel, J. Phys. Chem. 74 (1970) 4329–4335.
[71] A.B. Mukhopadhyay, C.B. Musgrave, J.F. Sanz, Atomic layer deposition of hafnium oxide from hafnium chloride and water, J. Am. Chem. Soc. 130 (2008) 11996–12006.
[72] C. Travis, R. Adomaitis, Modeling ALD surface reaction and process dynamics using absolute reaction rate theory, Chem. Vap. Depos. 19 (2013) 4–14.
[73] D.D. Koleske, S.M. Gates, Kinetics of atomic hydrogen + adsorbed Br reactions on Si (100) and Si(111) surfaces, J. Chem. Phys. 99 (1993) 8218–8228.
[74] C.C. Cheng, S.R. Lucas, H. Gutleben, W.J. Choyke, J.T. Yates Jr, Atomic hydrogen-driven halogen extraction from Si(100): Eley-Rideal surface kinetics, J. Am. Chem. Soc. 114 (1992) 1249–1252.
[75] J. Hong, A. Goullet, G. Turban, Optical characterization of hydrogenated amorphous carbon (a-C:H) thin films deposited from methane plasma, Thin Solid Films 364 (2000) 144–149.